Phys. Med. Biol., 1986, Vol 1, No. 3, 235-249. Printed in Great Britain

Electron beam dose distributions near standard inhomogeneities

K R Shortt, C K Ross, A F Bielajew and D W O Rogers

Division of Physics, National Research Council of Canada, Ottawa, Ontario, Canada K1A 0R6

Received 10 May 1985, in final form 14 October 1985

Abstract. At a recent workshop on electron beam dose planning, a set of standard geometries was defined to facilitate the comparison of electron beam treatment planning algorithms and dosimetric measurements. These geometries consist of one-, two- or three-dimensional inhomogeneities embedded near the entrance surface of a water phantom. In the three-dimensional case, the inhomogeneities are small cylinders of air or aluminium located on the beam axis. We have used a small (1 mm square by 0.1 mm thick) p-type silicon detector to measure the dose distributions behind these inhomogeneities for broad beams of 10 and 20 MeV electrons. The effect of the inhomogeneities is to perturb the dose in their vicinity by as much as 50% over a range of a few millimetres. These results provide a stringent test of techniques for calculating dose distributions. Current clinical algorithms do not accurately predict the dose distributions, but detailed Monte Carlo simulations are shown to be in good agreement with the experimental results.

1. Introduction

When a high-energy electron beam passes through matter, the electrons are scattered due to Coulomb interactions with the atomic nuclei. If the beam is intercepted by an inhomogeneity, i.e. a region of density or composition different from that of the surrounding material, the electrons will in general be scattered differently by the inhomogeneity than by the surrounding medium. As a result, the absorbed dose distribution may be strongly perturbed by the presence of an inhomogeneity. A number of measurements and calculations have been presented on this problem (e.g. Goitein 1978, Goitein *et al* 1978, Perry and Holt 1980).

The effects of electron scattering on the absorbed dose are most dramatic near the edge of an inhomogeneity where the lateral dose distribution exhibits a characteristic dip and peak over the range of a few millimetres. Behind an inhomogeneity whose density is greater than that of its surrounding medium there is an enhancement of the dose just outside its edge and a deficit in the dose just inside. This is because there are fewer electrons scattered in from the medium than scattered out from the high-density inhomogeneity. This situation is reversed for an inhomogeneity whose density is less than that of the surrounding medium. Behind it, the dose is enhanced inside its edge and decreased outside because more electrons are scattered in from the medium that are scattered out by the inhomogeneity.

Accurate dose planning algorithms for both electron beams and high energy photon beams must include the effects of electron scattering and energy loss. Current pencil beam algorithms (e.g. those of Perry and Holt (1980) and Hogstrom *et al* (1981)) can in principle handle three-dimensional inhomogeneities with the restriction that the dose contribution from each pencil is calculated as if the inhomogeneities are infinite

0031-9155/86/030235+15$02.50

in two dimensions. For regions downstream from a small air cavity, the pencil beam model of Perry and Holt (1980) quite accurately predicts the dose distribution. However, this approximate three-dimensional treatment is not yet common in clinics, and implementations of pencil beam models which handle only two-dimensional inhomogeneities lead to large errors for situations involving small three-dimensional inhomogeneities (Rogers *et al* 1984).

One of the outcomes of a 1982 workshop on electron beam dose planning (Brahme 1983) was the specification of a set of standard geometries to be used when comparing methods of measuring and calculating electron beam dose distributions. These geometries consist of one-, two- or three-dimensional inhomogeneities embedded near the surface of a water phantom. The three-dimensional geometry provides the most stringent test of any dose planning algorithm, and the primary motivation for the present work was to provide a set of measured dose distributions for this configuration.

Rogers *et al* (1984) have used the EGS Monte Carlo code (Ford and Nelson 1978) to calculate the dose distributions for the one- and three-dimensional standard geometries. Those calculations have now been extended to provide better spatial resolution for the three-dimensional geometry and the results are compared with the measured dose distributions.

2. Detector

Previous measurements of electron beam dose distributions near inhomogeneities show large dose variations over a distance of a few millimetres (Goitein *et al* 1978, Perry and Holt 1980). Accurate measurements therefore require a detector with good spatial resolution. We chose a silicon p–n junction as a dose detector, since spatial resolution of 1 mm or better and good sensitivity are easily achievable (Gager *et al* 1977, Rikner 1983, Rikner and Grussel 1983).

Rikner (1983) has shown that junctions constructed from n-type silicon have a response to radiation which decreases rapidly with accumulated dose and which is non-linear with dose rate. However, he found that p-type silicon does not suffer from these effects to the same degree. To our knowledge, there are no readily available commercial diodes constructed from p-type silicon, but pnp transistors are common, and we have tested a number of these as radiation detectors. With the emitter and collector electrically connected, we found that these devices behaved much like the custom built p-type diodes of Rikner.

We acquired some unmounted pnp transistor chips (referred to as Process 67 by National Semiconductor) about 1 mm square and mounted them on a low-mass support. Because of the masking on the chip, it was difficult to connect the emitter and collector together, so we have instead connected the base and emitter. Tests with packaged transistors showed that the device behaved similarly in either configuration.

The electronics used for measuring the junction signal and for monitoring the electron beam is shown in figure 1. The junction was operated with zero bias, and the reverse current was measured by a current integrator with a digital output. The junction leakage was about 50 pA, and was easily compensated with the integrator offset adjustment. At our typical dose rate of 30 Gy min^{-1} the peak junction signal was roughly 1 nA. The electron beam was monitored with a parallel-plate ion chamber read by a second current integrator. The digital outputs from both integrators were fed to CAMAC scalers interfaced to a PDP 11/60 computer. For most measurements adequate precision (1%) was obtained by allowing the scalers to count for 5 s.

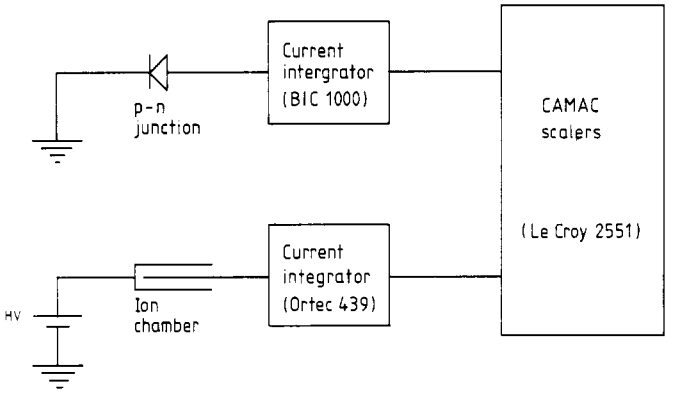

Figure 1. Block diagram of the electronics used to measure the current from the silicon p-n junction detector and the ion chamber monitor. The CAMAC scalers were interfaced to a PDP 11/60 computer.

A number of preliminary measurements to investigate the behaviour of our detector will be reported in a separate publication and will only be mentioned here. Firstly, care was required to ensure that the detector response was independent of the orientation of the silicon chip with respect to the beam. Unmodified commercial diodes exhibit a strong orientation effect due to perturbation of the electron fluence by the rather massive leads used to make electrical contact. Our usual 'face-on' configuration had the beam direction normal to the 1 mm^2 surface. Rotation of the detector through 90° to the 'edge-on' orientation gave identical results indicating that our low-mass supporting structure did not perturb the electron fluence.

Secondly, we examined the effect of dose rate on the detector response. Both the detector and ion chamber monitor outputs were measured as the electron beam current was varied. After correcting for ion chamber saturation effects, the detector response

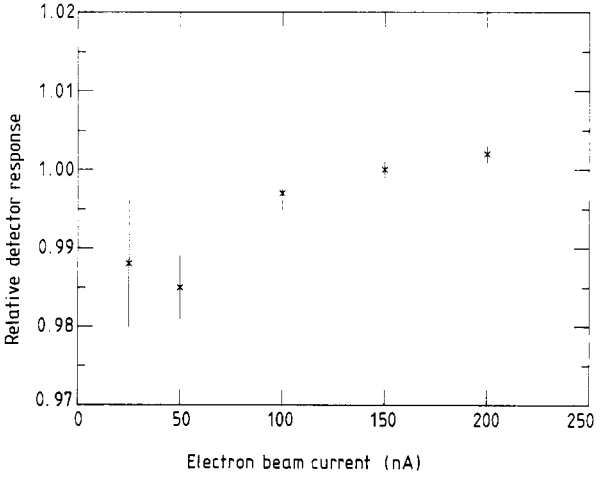

Figure 2. Silicon p-n junction detector response relative to the response of the ion chamber monitor, as a function of electron current at 20 MeV. The ion chamber data were corrected for recombination losses. The error bars are an estimate of the uncertainty due to the finite number of counts registered during the 5 s counting interval. A current of 150 nA corresponded to a dose rate of about 0.5 Gy s^{-1} at the detector position.

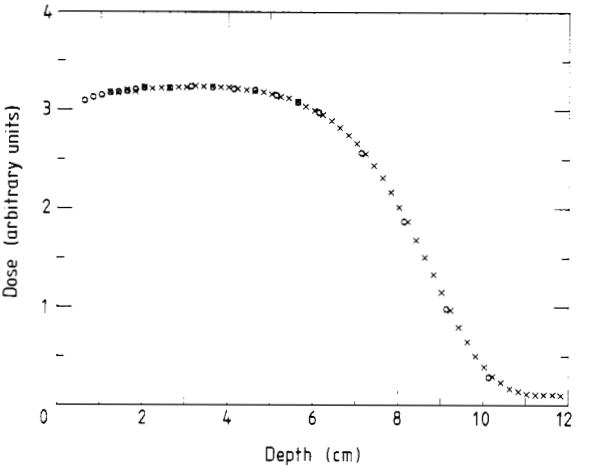

Figure 3. Comparison of the depth-dose distribution (○) derived from the depth-ionisation response of a parallel-plate ion chamber to the response (×) of the silicon p-n junction detector as a function of depth. No correction has been applied for the water to silicon stopping power ratio.

relative to that of the ion chamber was calculated, and the results are shown in figure 2. Although there may be a small increase (1%) in detector sensitivity with dose rate, we concluded that for the present set of measurements this effect could safely be ignored.

Finally, we needed to relate the detector response to the absorbed dose to water. Using a parallel-plate ion chamber (Capintec model PS-033) we measured the ion chamber response as a function of depth in a homogeneous water phantom irradiated with 20 MeV electrons. Using the stopping power ratio of water to air (AAPM 1983) the ion chamber data were converted to give the depth-dose distribution shown in figure 3. The response of our silicon detector was normalised to the depth-dose data at 4 cm. Over most of the depth-dose distribution the detector response is proportional to absorbed dose. This result is consistent with the fact that the water to silicon collisional stopping power ratio changes by only 2% between 20 MeV and 3.5 MeV (ICRU 1984).

3. Experimental set-up

The standard inhomogeneity geometries have been defined for one, two and three dimensions (Brahme 1983). We have concentrated on the three-dimensional case since it provides a very stringent test of dose planning algorithms. The recommended phantom material is water, and the inhomogeneities to be introduced are small cylinders of air or aluminium. Either cylinder is to be 1 cm in diameter, and 2 cm long if air, or 1 cm long if aluminium. The cylinders should be on the beam axis, either 2 mm or 2 cm deep in the water phantom. The source to phantom distance should be 100 cm, and recommended electron energies are 10 and 20 MeV.

An overview of our irradiation geometry is shown in figure 4. An electron beam from the NRCC linac passed through an energy-analysing magnet (not shown) and emerged through a 0.13 mm thick titanium exit window. The beam position and profile were monitored during set-up by a rotating wire beam profile monitor (a modified National Electrostatics Corporation unit) located about 10 cm upstream from the exit window. The beam profile was approximately Gaussian in shape with a full width at half maximum of 3 to 4 mm. The electron beam passed through a lead scattering foil 0.13 mm thick and impinged on the water phantom 103 cm downstream from the foil.

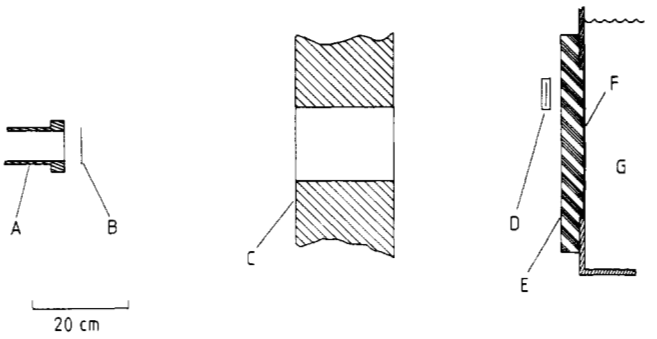

Figure 4. Irradiation geometry. The principal components are identified by letters: A, beam line from the electron accelerator. The exit window is 0.13 mm thick titanium; B, 0.13 mm thick lead scattering foil; C, iron collimator; D, parallel-plate ion chamber used to monitor the electron beam. It was located about 10 cm off the beam axis; E, 3.9 cm thick Styrofoam slab used to support the entrance window; F, 0.13 mm thick Kapton window; G, water phantom. The Styrofoam and Kapton window together have an equivalent thickness of 0.13 cm of water. The effective depth in water is the physical depth plus this 0.13 cm.

The beam was monitored by a parallel-plate ion chamber located about 10 cm off the beam axis so as to minimise its effect on the incident beam.

The water phantom consisted of a Lucite tank, approximately 50 cm on each side. The beam entered the tank through a 30 cm diameter, 0.13 mm thick Kapton window (density of 1.42 g cm^{-3}). In order to keep the entrance face reasonably flat (±1 mm), the Kapton window was supported by a Styrofoam plate (density of 0.028 g cm^{-3}) 3.9 cm thick.

The detector position in the water phantom was determined by a three-dimensional translator interfaced to a PDP 11/60 computer. Using a precision gauge block and a survey telescope, the depth scale was calibrated absolutely. Detector positioning was found to be reproducible to within 0.1 mm.

The aluminium cylinder used for our measurements had a diameter of 1.004 cm, a length of 0.998 cm and density of 2.65 g cm^{-3}. Several different air cavities were used throughout our measurements. They were all constructed from 0.13 mm thick Kapton sheet, and had internal dimensions of 1.03 ± 0.01 cm (diameter) by 2.00 ± 0.03 cm (length).

The Kapton entrance window and Styrofoam are equivalent to 0.13 cm of water and all depth measurements are made relative to 'the effective water surface'. We have mounted the aluminium and air cylinders directly on the Kapton window when setting up the 2 mm geometries. This amounts to an effective 'depth' of 1.3 mm. For the 2 cm geometries, the cylinders were mounted 2 cm deep in the water at an effective 'depth' of 2.13 cm. In this case, each cylinder was supported on a Kapton stand-off identical to our air cylinders, but filled with water.

4. Irradiation conditions

The energy of our electron beam was obtained from depth-ionisation measurements using a parallel-plate ion chamber (Capintec model PS-033). The extrapolated range, R_p, from the depth-ionisation curves was used to calculate the most probable energy $E_{p,0}$, at the effective surface of the water phantom using the Nordic protocol (NACP 1980). For our nominal 10 MeV energy we obtained $R_p = 5.05 \pm 0.02$ cm and $E_{p,0} = 10.28 \pm 0.04$ MeV, while for the nominal 20 MeV energy, $R_p = 10.11 \pm 0.03$ cm and $E_{p,0} = 20.49 \pm 0.06$ MeV.

In order further to specify our irradiation geometry, we have determined the position of the virtual point source. Although the pinhole plate technique has been recommended for this measurement (Schroder-Babo 1983) it is diffcult to construct such a plate. Instead, we used a 1 cm thick lead plate in which two parallel slots, 4 mm wide, 4 cm long and separated by 5 cm, were machined at an angle roughly matched to the beam divergence. The plate was located 64 cm downstream from the scattering foil and the silicon detector was scanned in the empty water phantom at right angles to the slots. By using similar triangles, the mean position of the virtual source was found to be 6.9 ± 3.0 cm upstream of the scattering foil for the 10 MeV beam and 2.2 ± 1.5 cm for the 20 MeV beam.

During irradiation we expected the detector response per unit dose to decrease due to radiation damage. We therefore defined a point 5 cm off the beam axis and 2 cm deep for the 10 MeV beam and 4 cm deep for the 20 MeV beam as a normalisation point. We measured the response at this checkpoint before every scan and corrected the data accordingly. During the complete set of irradiations the detector response decreased by only 7%.

5. Monte Carlo simulations

The Monte Carlo calculations were performed using the EGS code. A complete description of the physical processes covered in the simulation is contained in Ford and Nelson (1978) and a brief overview has been given by Rogers (1982). The calculations have been done using version 4 of the code which has been corrected for use at energies of interest to medical physics (Nelson *et al* 1985). The transport parameters (as defined in Rogers 1984) were as follows:

(i) ECUT = 700 keV total energy—no electron was transported below 189 keV kinetic energy;

(ii) AE = 700 keV total energy—no δ-ray was created below 189 keV kinetic energy;

(iii) PCUT = 100 keV—no photon was transported below 100 keV;

(iv) AP = 100 keV—no bremsstrahlung photon below 100 keV was set in motion;

(v) ESTEPE = 4% for all the 20 MeV cases and the homogeneous 10 MeV cases; 2% for the 10 MeV inhomogeneous cases.

In addition, the maximum step size was restricted to 0.5 cm. Rogers (1984) has shown that there is not a strong dependence on electron step size at these energies in homogeneous media. However, care was taken to ensure that the step sizes were sufficiently small for the inhomogeneous cases to avoid calculational artefacts described elsewhere (Bielajew *et al* 1985).

The calculations simulated monoenergetic 10 or 20 MeV electrons from a point source in a vacuum 100 cm away from the front face of the water phantom. Auxillary Monte Carlo calculations were performed to examine the effect of the beam exit window, lead scattering foil and air on the electron energy spectrum. At 10 MeV, the mean electron energy at the effective surface of the water phantom was calculated to be 0.35 MeV less than the most probable energy, while at 20 MeV the difference was 0.65 MeV. Thus, from a comparison with the most probable energies, the mean energies at the 'effective' phantom surface were 9.93 MeV and 19.84 MeV. Since various dosimetry protocols use different methods for specifying the beam energy, we are reporting both the mean energy and the most probable energy.

The standard inhomogeneities described in § 3 were situated on-axis at a depth of 0.2 or 2.0 cm. A cylindrical-planar geometry was used with an outer phantom

radius of 5.0 cm and a total depth of 10.5 cm (10 MeV case) or 21 cm (20 MeV case). These phantom dimensions were essentially infinite as far as the dose distributions near the inhomogeneities were concerned. Electrons below 6 MeV were not followed if their range was less than the distance to any region where the dose profile was desired. This range rejection technique is an approximation in that the bremsstrahlung component of the dose is not completely modelled, but it produces a negligible error in the calculated dose near the inhomogeneities.

The central axis bins were 0.25 cm in radius and about 0.25 cm (10 MeV case) or 0.5 cm (20 MeV case) in the beam direction. For the inhomogeneous cases the bin thickness was reduced to 0.10 cm (10 MeV case) or 0.20 cm (20 MeV case) at the position where the radial profile was required. The central axis results in the inhomogeneous cases are susceptible to bin size effects due to averaging in the vicinity of the inhomogeneity because the dose is a strong function of the radial position. However, computing times become excessive if the bin radius is made much less than 0.25 cm. The computing time required for the results presented in this study was about 200 h on a VAX 11/780. Central axis results have a statistical accuracy of about ±2%. The incident electrons were restricted to a solid angle defined by the entrance face of the phantom, and about 500 000 incident electrons were required for each of the ten simulations.

6. Results

At each energy and for each geometry a depth-dose scan was done, as well as a number of scans at right angles to the beam direction. The 10 MeV results are summarised in figures 5–10 while the corresponding data at 20 MeV are shown in figures 11–16. Note that the experimental data for all the inhomogeneous cases have been shifted slightly along the depth axis. In doing this, we are able to compare the experimental data and the calculations at the same distance behind the inhomogeneity. In the 2 mm cases, this shift amounts to 0.7 mm away from the surface and in the 2 cm cases, the shift is 1.3 mm closer to the surface. The measured radial dose profiles (not shown) for the homogeneous water phantom were flat to within ±2% over a 2 cm radius about the central axis and would join the wings shown on the experimental data.

The vertical scale of figures 5–16 is the calculated dose divided by the incident fluence at the centre of the front face of the water phantom. The measured data were normalised to the calculated dose at the peak of the central axis depth-dose distribution for the homogeneous water phantom. Thus only one normalisation factor was used for each energy.

The basic effects of electron scattering on the dose distribution behind the edge of an inhomogeneity have been discussed in the introduction. These effects give rise to the characteristic dips and peaks we see in the dose distribution behind the air and aluminium cylinders (e.g. figures 12 and 13).

Overall, the agreement between the measured and calculated dose distributions is very good. However, there were some differences between the experimental configuration and the model system which must be considered in a detailed comparison. Firstly, the model calculations did not include the scattering foil, the collimator or the air between the foil and the water phantom. Secondly, for the measurements the inhomogeneities were mounted at effective depths of 0.13 and 2.13 cm instead of the 0.2 and 2.0 cm depths used in the calculations. Finally, the electron energies for the calculations were exactly 10 MeV and 20 MeV whereas for the measurements,

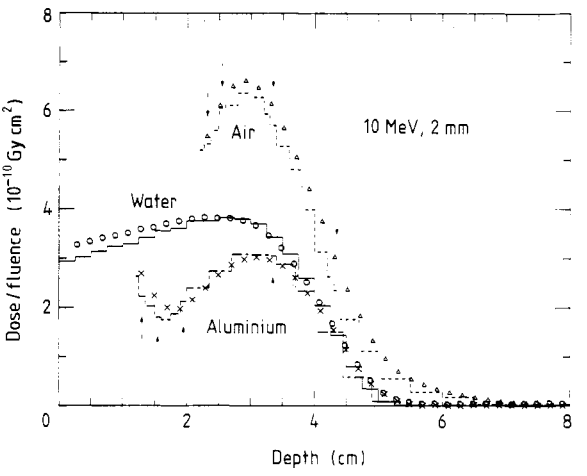

Figure 5. Depth-dose distributions obtained with 10 MeV electrons incident on the water phantom with the standard inhomogeneities mounted on the entrance window (2 mm geometry). The symbols represent the measured data as follows: ○, homogeneous water phantom; ×, aluminium cylinder; △, air cylinder. The histograms are the results of the Monte Carlo calculations. For the homogeneous case and all the calculations, the depth is from the effective water surface (including the 1.3 mm water-equivalent walls). For the inhomogeneous cases, the measured data have been shifted 0.7 mm deeper to have the inhomogeneities aligned with those in the calculations. The arrows show depths at which radial profiles are presented in the next two figures. The units on the vertical axis are in terms of absorbed dose to water per unit incident fluence of 10 MeV electrons. The measured results were normalised to the calculated values as described in the text. The measurements have a precision of about ±1%, while the statistical accuracy of the Monte Carlo results is about ±2%.

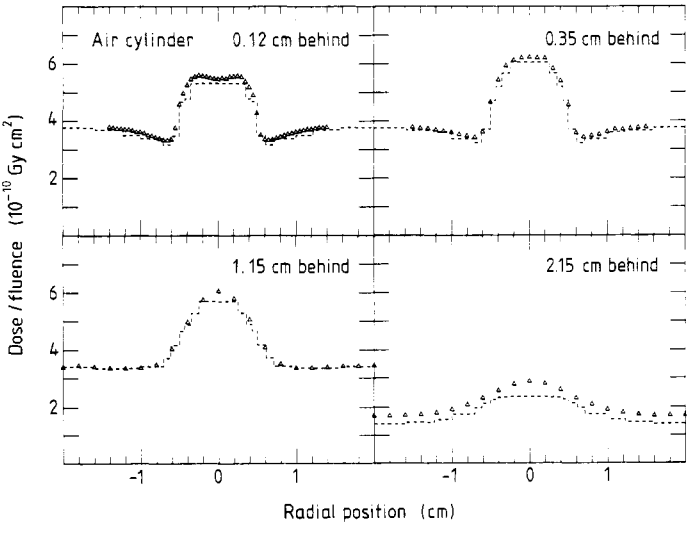

Figure 6. Radial dose profiles for 10 MeV electrons incident on the standard air cylinder mounted on the entrance window of the water phantom (2 mm geometry). The symbols represent the measured data, and the histograms are the Monte Carlo results. The depths of the experimental data have been adjusted (0.7 mm deeper) to give the same distances past the inhomogeneities as in the calculation. Far from the inhomogeneities, this shift can cause an apparent discrepancy between the experimental data and the calculation as discussed in § 6. The measurements have a precision of about ±1%, while the statistical accuracy of the Monte Carlo results is about ±2%.

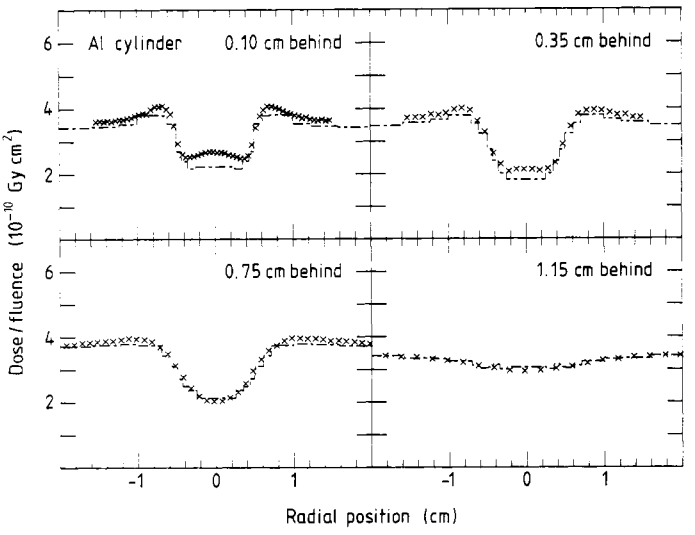

Figure 7. Same as figure 6, but for the standard aluminium cylinder.

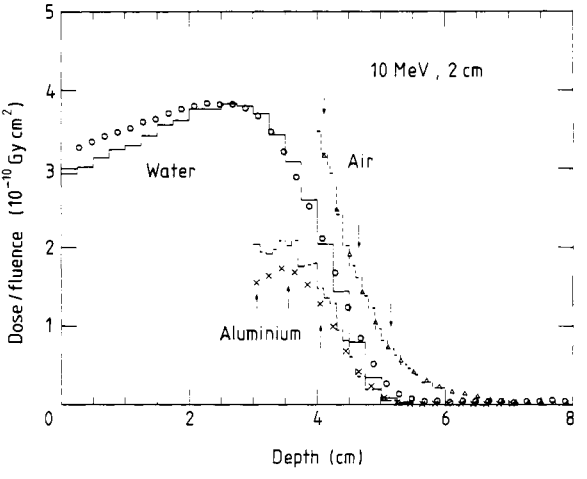

Figure 8. Same as figure 5, but with the standard cylinders mounted at a depth of 2 cm in the water phantom (2 cm geometry). The depths of the experimental data have been adjusted (1.3 mm shallower) to give the same distances past the inhomogeneities as in the calculation.

the corresponding most probable energies at the surface of the phantom were 10.28 MeV and 20.49 MeV and the corresponding mean energies were 9.93 and 19.84 MeV.

Regarding the second point, we have attempted to allow for the differences in the locations of the inhomogeneities when comparing the measured and calculated results. Since the perturbation in the dose distribution near an inhomogeneity is more sensitive to the distance behind the inhomogeneity than to the depth in the water phantom, the measured and calculated doses in the inhomogeneous cases are compared at the same distance behind the inhomogeneity rather than at the same depth in the water phantom. This means the measured data are shifted in depth +0.7 mm and −1.3 mm in the 2 mm and 2 cm cases respectively. Unfortunately, this leads to an apparent discrepancy in the wings of the dose profiles where the dose is not perturbed by the inhomogeneity and

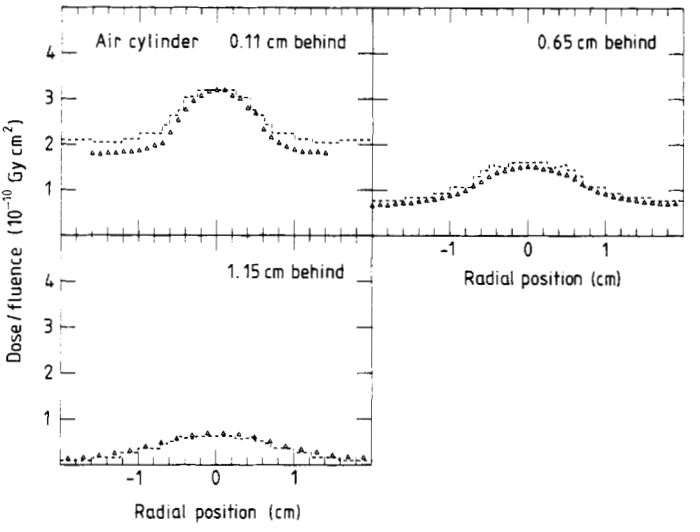

Figure 9. Same as figure 6, but with the air cylinder at a depth of 2 cm in the water phantom (2 cm geometry). The depths of the experimental data have been adjusted (1.3 mm shallower) to give the same distances past the inhomogeneities as in the calculation.

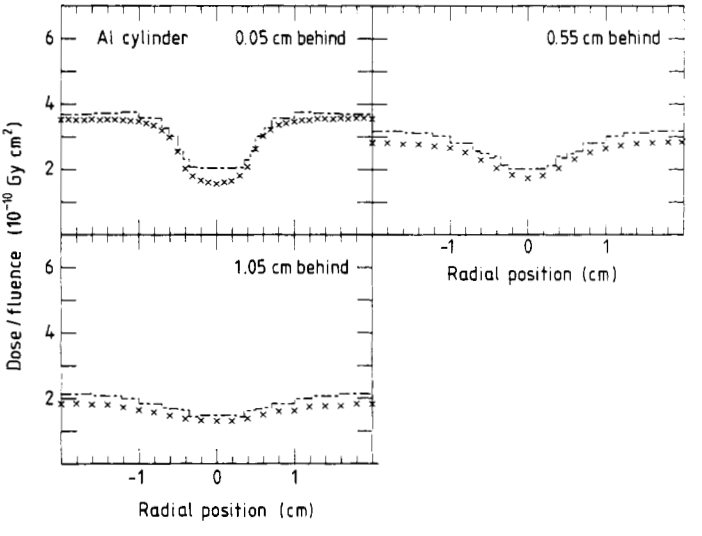

Figure 10. Same as figure 9, but for the standard aluminium cylinder.

where it depends only on the depth. For example, in figure 9 for the 10 MeV beam in the 2 cm geometry the calculated results appear to be about 16% higher than the experimental data in the wings of the dose profile 1 mm behind the air cylinder. Remembering that the dose gradient at this depth in the homogeneous case is about 12% per mm along the central axis and recognising that in the wings away from the inhomogeneity the gradient ought to be at least that large, the 1.3 mm shift accounts for this apparent discrepancy. In other cases the discrepancy is not so large because the depth-dose curve is flatter at those depths. In the 2 mm case the apparent discrepancy would be in the opposite sense because the shift is in the other direction.

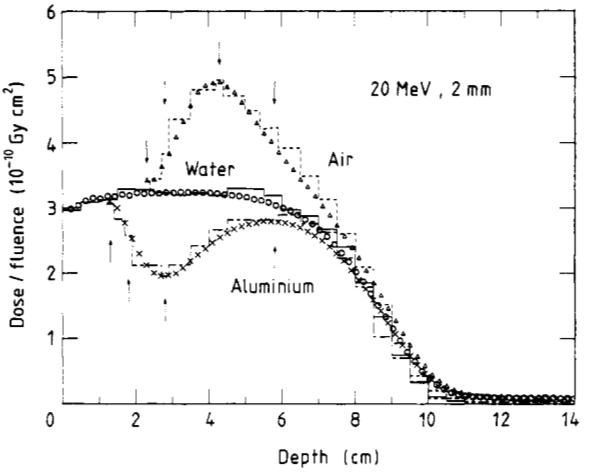

Figure 11. Depth-dose distributions obtained with 20 MeV electrons incident on the water phantom with the standard inhomogeneities mounted on the entrance window (2 mm geometry). The symbols represent the measured data as follows: ○, homogeneous water phantom; ×, aluminium cylinder; △, air cylinder. The histograms are the results of the Monte Carlo calculations. For the homogeneous case and all the calculations, the depth is from the effective water surface (including the 1.3 mm water-equivalent walls). For the inhomogeneous cases, the measured data have been shifted 0.7 mm deeper to have the inhomogeneities aligned with those in the calculations. The arrows show depths at which radial profiles are presented in the next two figures. The units on the vertical axis are in terms of absorbed dose to water per unit incident fluence of 20 MeV electrons. The measured results were normalised to the calculated values as described in the text. The measurements have a precision of about ±1%, while the statistical accuracy of the Monte Carlo results is about ±2%.

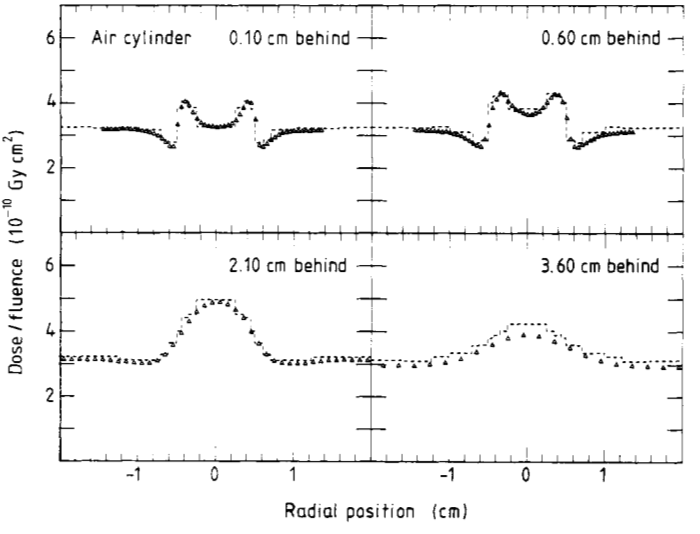

Figure 12. Radial dose profiles for 20 MeV electrons incident on the standard air cylinder mounted on the entrance window of the water phantom (2 mm geometry). The symbols represent the measured data, and the histograms are the Monte Carlo results. The depths of the experimental data have been adjusted (0.7 mm deeper) to give the same distances past the inhomogeneities as in the calculation. Far from the inhomogeneities, this shift can cause an apparent discrepancy between the experimental data and the calculation as discussed in § 6. The measurements have a precision of about ±1%, while the statistical accuracy of the Monte Carlo results is about ±2%.

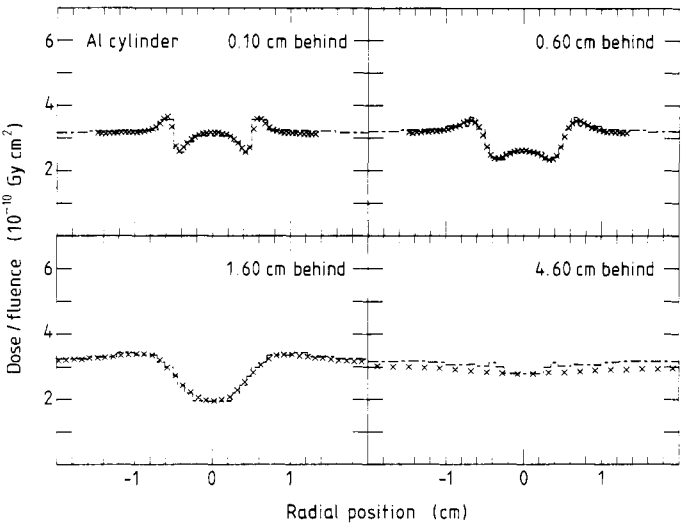

Figure 13. Same as figure 12, but for the standard aluminium cylinder.

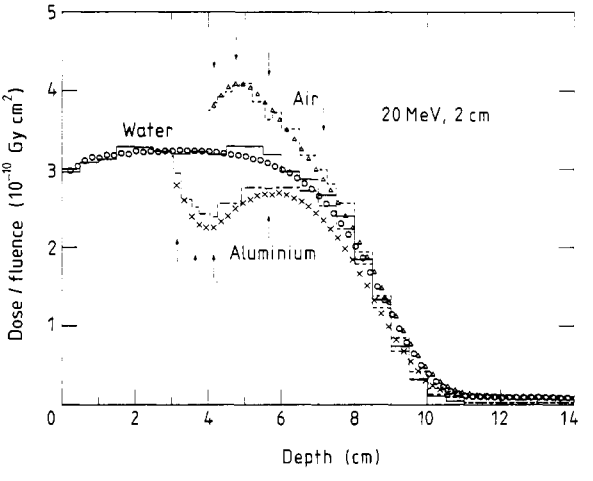

Figure 14. Same as figure 11, but with the standard cylinders mounted at a depth of 2 cm in the water phantom (2 cm geometry). The depths of the experimental data have been adjusted (1.3 mm shallower) to give the same distances past the inhomogeneities as in the calculation.

In order to check the effect of the Kapton walls of our air cylinders on the dose distributions, measurements were performed behind a cylinder filled with water. The resulting dose distributions were not measurably different from those obtained for the homogeneous water phantom.

Most of our measurements were done with the resolution of the electron beam energy-analysing magnet set to ±1.5% (this corresponds to ±0.15 MeV at 10 MeV and ±0.30 MeV at 20 MeV). In order to check the effect of the energy resolution on the dose distributions, measurements were performed for a number of slit settings on the energy-analysing magnet. For 20 MeV electrons incident on a homogeneous phantom, the depth-dose distributions were unaffected when the energy resolution was improved from ±1.5% to ±0.5%.

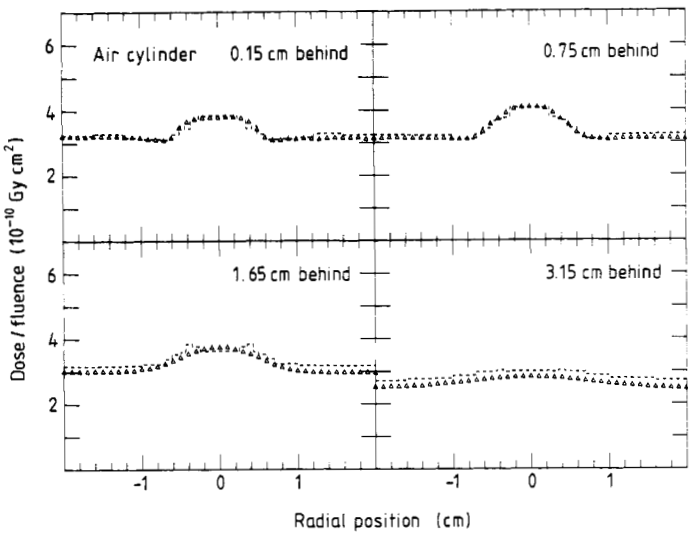

Figure 15. Same as figure 12, but with the air cylinder mounted at a depth of 2 cm in the water phantom (2 cm geometry). The depths of the experimental data have been adjusted (1.3 mm shallower) to give the same distances past the inhomogeneities as in the calculation.

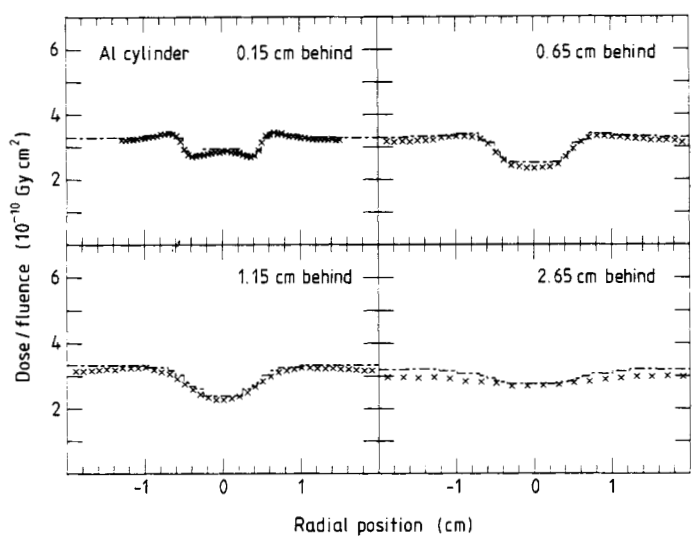

Figure 16. Same as figure 15, but for the standard aluminium cylinder.

The measured and calculated 10 MeV depth-dose distributions for the homogeneous water phantom differ by about 8% near the surface of the water phantom (figure 5). The measured results are larger than the calculated values, which might suggest the presence of low energy electrons in the incident beam. In order to check this possibility, measurements were done with the lead scattering foil and the iron collimator removed. Although the radial dose distributions were somewhat less flat, the shape of the depth-dose distribution was not significantly different. Since the measured and calculated results were arbitrarily normalised at the peak of the depth-dose distribution, it is not certain that the discrepancy should be attributed to the surface region. The

slopes of the measured and calculated results are approximately the same between 0 and 1.5 cm, and if the normalisation were performed in this region, the discrepancy would be transferred to the falling edge of the depth-dose distribution.

7. Summary

In order to facilitate the comparison of electron beam dose planning algorithms, a set of standard geometries has been defined (Brahme 1983). We have measured the dose distributions for the complete set of three-dimensional geometries.

To achieve the required spatial resolution (1 mm or better) we used a silicon p-n junction as a detector. Rikner (1983) has shown that detectors in which the bulk of the material is p-type silicon have superior characteristics as radiation detectors to those in which it is n-type. This suggested the use of a pnp transistor chip with the base and emitter electrically connected as the basis for our detector. The transistor was mounted on a low mass support, and the resulting detector showed no dependence on its orientation with respect to the incident beam. This gave us confidence that the detector was not significantly perturbing the electron fluence in the water phantom.

We have presented depth-dose distributions at 10 and 20 MeV, as well as radial dose profiles at selected distances behind the inhomogeneities. Dose variations as large as 50% over the range of a few millimetres were observed. The irradiation conditions have been carefully specified, so these results should serve as a useful benchmark for testing dose planning algorithms.

The results of detailed Monte Carlo calculations based on the EGS code are compared with the measured dose distributions. The agreement is very good, giving added confidence in the ability of Monte Carlo calculations to cope properly with complicated geometries.

Acknowledgments

We wish to express our appreciation to George Smith, who developed the techniques for mounting our detectors and to Alex Nowak for the operation of the linear accelerator.

Résumé

Distributions de dose dans les faisceaux d'électrons au voisinage des hétérogénéités.

Au cours d'un réunion récente d'un groupe de travail sur la détermination des doses dans les faisceaux d'électrons, il a été défini des conditions de géométrie standard permettant de faciliter la comparaison des algorithmes de calcul pour les distributions de dose dans les faisceaux d'électrons et les résultats expérimentaux. Cette géométrie consiste en des hétérogénéités à une, deux ou trois dimensions incluses dans un fantôme d'eau au voisinage de la surface d'entrée. Les hétérogénéités à trois dimensions sont constituées de petits cylindres d'air ou d'aluminium placés sur l'axe du faisceau. Nous avons utilisé un petit détecteur au silicone de type p (de section carrée de 1 mm × 1 mm et 0,1 mm de haut) pour mesurer les distributions de dose derrière ces hétérogénéités pour des faisceaux larges d'électrons de 10 et 20 MeV. Les hétérogénéités ont pour effet de créer une perturbation sur la dose dans leur voisinage, pouvant aller jusqu'à 50% sur quelques millimètres. Ces résultats constituent un test rigoureux pour les techniques de calcul des distributions de dose. Les algorithmes utilisés couramment en clinique ne permettent pas de prévoir de façon précise les distributions de dose, mais les méthodes par simulation de Monte Carlo conduisent à des résultats en bon accord avec les données expérimentales.

Zusammenfassung

Dosisverteilungen in der Nähe von Standardinhomogenitäten bei Elektronenstrahlung.

Vor kurzem fand ein Workshop über die Bestrahlungsplanung bei Elektronenstrahlung statt, in dessen Verlauf eine Reihe von Standardgeometrien definiert wurden, um den Vergleich zwischen Bestrahlungsplanungsverfahren bei Elektronenstrahlung und dosimetrischen Messungen zu erleichtern. Diese Geometrien bestehen aus ein-, zwei- und dreidimensionalen Inhomogenitäten, die nahe der Eintrittsfläche eines Wasserphantoms gelagert sind. Im dreidimensionalen Fall bestehen die Inhomogenitäten aus kleinen Zylindern aus Luft oder Aluminium, die auf der Strahlachse liegen. Zur Messung der Dosisverteilung hinter diesen Inhomogenitäten wurde für große Felder und Elektronen mit einer Energie von 10 und 20 MeV ein kleiner (1 mm × 1 mm bei 0.1 mm Dicke) Siliziumdetektor vom p-Typ verwendet. Die Inhomogenitäten stören in ihrer Umgebung die Dosisverteilung um 50% in einem Bereich von wenigen Millimetern. Mit Hilfe dieser Ergebnisse können Verfahren zur Berechnung von Dosisverteilungen überprüft werden. Die gebräuchlichen klinischen Verfahren sagen die Dosisverteilung nicht genau voraus; es wird aber gezeigt, daß die Ergebnisse ausführlicher Monte Carlo-Rechnungen gut mit den experimentellen Ergebnissen übereinstimmen.

References

AAPM 1983 *Med. Phys.* **10** 741-71

Bielajew A F, Rogers D W O and Nahum A E 1985 *Phys. Med. Biol.* **30** 419-27

Brahme A 1983 *Acta Radiol. Suppl.* **364** 101-2

Ford R L and Nelson W R 1978 *Stanford Linear Accelerator Center Report* 210

Gager L D, Wright A E and Almond P R 1977 *Med. Phys.* **4** 494-8

Goitein M 1978 *Med. Phys.* **5** 257-64

Goitein M, Chen G T Y, Ting J Y, Schneider R J and Sisterson J M 1978 *Med. Phys.* **5** 265-73

Hogstrom K R, Mills M D and Almond P R 1981 *Phys. Med. Biol.* **26** 445-59

ICRU 1984 *Stopping Powers for Electrons and Positrons* Report 37 (Bethesda, MD: ICRU)

NACP 1980 *Acta Radiol.* **19** 55-79

Nelson W R, Hirayama H and Rogers D W O 1985 *The EGS System, Version 4, Stanford Linear Accelerator Center Report* 265

Perry D J and Holt J G 1980 *Med. Phys.* **7** 207-15

Rikner G 1983 *PhD Dissertation* Uppsala University

Rikner G and Grussell E 1983 *Phys. Med. Biol.* **28** 1261-7

Rogers D W O 1982 *Nucl. Instrum. Meth.* **199** 531-48

——1984 *Nucl. Instrum. Meth.* A **227** 535-48

Rogers D W O, Bielajew A F and Nahum A E 1984 *Proc. 8th Int. Conf. on Use of Computers in Radiation Therapy, Toronto* (Silver Spring, MD: IEEE) pp 140-4

Schroder-Babo P 1983 *Acta Radiol. Suppl.* **364** 7-10